Multistage Nanovehicle Delivery System Based on Stepwise Size Reduction and Charge Reversal for Programmed Nuclear Targeting of Systemically Administered Anticancer Drugs

*Lian Li, Wei Sun, Jiaju Zhong, Qingqing Yang, Xi Zhu, Zhou Zhou, Zhirong Zhang, and Yuan Huang**

The nucleus is the final target of many first-line chemotherapeutics, but the need to overcome multiple physiological barriers imposes conflicting requirements for size and charge on systemically administered drug delivery systems. Here, an *N*-(2-hydroxypropyl) methacrylamide (HPMA) polymer-based nanovehicle (PNV) that self-assembles from anionic HPMA copolymers with charge-reversal ability and cationic HPMA copolymers with intracellularly detachable subgroups (IDS) is described. The IDS, bearing an anticancer drug and nuclear-homing cell-penetrating peptide (R8NLS ligand), is grafted onto the HPMA copolymer via hydrazone linkage. The large, neutrally charged, self-assembled PNV (≈55 nm) shows good blood persistence and preferential tumor accumulation. After tumoral arrival, the extracellular milieu actuates the disassembly of PNV to linear conjugates (≈10 nm/39 kDa). This first-stage size reduction exposes R8NLS and allows for deeper tissue penetration and greater cellular internalization. After endocytosis, a second-stage size reduction occurs when the more acidic endolysosomal pH cleaved the ≈2.4 kDa IDS off the HPMA copolymer backbone and guaranteed the successful nuclear entry via nuclear localization signal assistance. Based on the stepwise size reduction and on-demand R8NLS exposure, the PNV inhibits growth of HeLa tumors in nude mice by 75%. This work gives important insights into the design of systemic nuclear-targeted delivery via a multistage size/charge changing way.

1. Introduction

The nucleus is the pharmacological target of many first-line chemotherapeutics. Unfortunately, effectively delivering these drugs to nucleus is challenged by ubiquitous barriers, and often plagued with issues of rapid renal excretion, unwanted mononuclear phagocyte system (MPS) elimination, insufficient tumor penetration, poor cell internalization, undesirable lysosomal sequestration, and nuclear envelope segregation.[1] Studies have succeeded in overcoming one or two of these obstacles, but any one of the remaining barriers can be an Achilles' heel that profoundly decreases the final drug concentration in the nucleus. Worse still, developing a nanovehicle that conquers all known barriers remains a huge challenge, in part because the requirements for particle size/surface charge of a nanovehicle in a series of physiological processes are contradictory.[2]

Generally, there is a decreasing "size ladder" criteria for the transport of nanoparticles from blood to tumor cancer nucleus. Large nanocarriers with size range of 50–200 nm can spontaneously accumulate around leaky regions of the tumor vasculature via the "enhanced permeability and retention" (EPR) effect.[3] However, the tumor extracellular matrix consisting of an interconnected network of collagen fibers blocks penetration of these large nanoparticles, leaving them primarily trapped in perivascular regions.[4] It has been found reducing the particle size could lower the diffusional hindrance in the tumor interstitial space and gives a better tumor distribution.[5] In this regard, a moderately smaller size (10–20 nm) is expected to be optimal, as it is sufficiently small to penetrate deep into tumor tissue, meanwhile, large enough to have slower tumor clearance than small-molecular drugs.[5,6] Upon the arrival of cancer cell cytoplasm, passive transport of macromolecules to nucleus remains a bottleneck,[7] which is largely dictated by the nanoparticle size[8] or copolymer molecular weight[9] due to nucleopore threshold (<9 nm). Gold nanoparticles of only 2 and 6 nm, but not larger (10 and 15 nm), were found to localize in nucleus.[8b] However, the same small size that ensures nuclear penetration would also undergo rapid kidney excretion in vivo, leading to restrictive tumor accumulation.[10] Since nuclear

Dr. L. Li, W. Sun, J. Zhong, Dr. Q. Yang, Dr. X. Zhu,
Dr. Z. Zhou, Prof. Z. Zhang, Prof. Y. Huang
Key Laboratory of Drug Targeting
and Drug Delivery System
Ministry of Education
West China School of Pharmacy
Sichuan University
No. 17, Block 3, Southern Renmin Road, Chengdu 610041, P. R. China
E-mail: huangyuan0@163.com

DOI: 10.1002/adfm.201501248

localization signal (NLS) can trigger intranuclear entry of nanovehicle even moderately larger than nucleopore threshold, several nucleus-targeted delivery strategies have been developed via the surface decoration with NLS peptides.[11] While these methods can target drugs to the nucleus in vitro, they may not be relevant for in vivo delivery, as the cationic charge conferred by the NLS is a double-edged sword. On one hand, it is essential for the ligands' nuclear-homing capability;[1c] on the other hand, it suffers from nonspecific tissue distribution and rapid body clearance.[12]

In this way, the two crucial dispensabilities (small particle size and cationic NLS grafting) for nuclear targeting are exactly the opposite requirements for the in vivo application, which might explain that only limited nuclear-targeted designs have yet been translated to systemic administration. Among these few instances, a sequential vascular-to-cell nuclear-targeted drug delivery platform was designed via dual-ligand modification, in which the arginine-glycine-aspartic (RGD) peptide targets tumor vascular and transactivator of transcription (TAT) peptide mediates nuclear localization.[13] The main concern with this system is that the premature penetration of TAT can override the targeting effect of RGD. To shield the cationic charges of TAT, 75 nm micelles functionalized with charge-reversible TAT were prepared by temporarily amidizing the lysine residue amines.[7b] Despite their selective tumor accumulation, the micelle was only found to dock at nucleopores but not passing through, because of its large size. Besides, the direct modification of TAT ligand can also deactivate the ligand.[1c]

These previous studies make clear the need to satisfy two pairs of conflicting requirements for efficient in vivo nuclear delivery. One is that the nanovehicle must gradually shrink in size from its circulation in blood to its arrival at the nucleus. It should be relatively large in order to trigger the EPR effect, then smaller to lower the diffusional hindrance for tumor penetration and then smaller again to pass through the nucleopore. The second requirement is that the cationic charge of active targeting ligands should be concealed to avoid premature tissue penetration in circulation, but re-exposed to facilitate cell internalization and nuclear uptake after tumor arrival.

To advance beyond current strategies, we proposed a new direction for systemic nuclear targeting strategy, in which the size and charge of the nanovehicle system could be transformable by adapting to the varying barriers in a multistage stimuli-responsive way (**Figure 1**). The *N*-(2-hydroxypropyl) methacrylamide (HPMA) polymer-based nanovehicle (PNV) self-assembles from two oppositely charged copolymers: anionic copolymer with charge-reverse ability and cationic copolymer containing intracellularly detachable subgroup (IDS). The IDS consists of a model drug and a tandem fusion of cell-penetrating peptide (CPP) (octaarginines peptide, R8) and an NLS (R8NLS). We hypothesized that the original PNV with the neutralized charge and enlarged size tailored for increasing EPR effect would

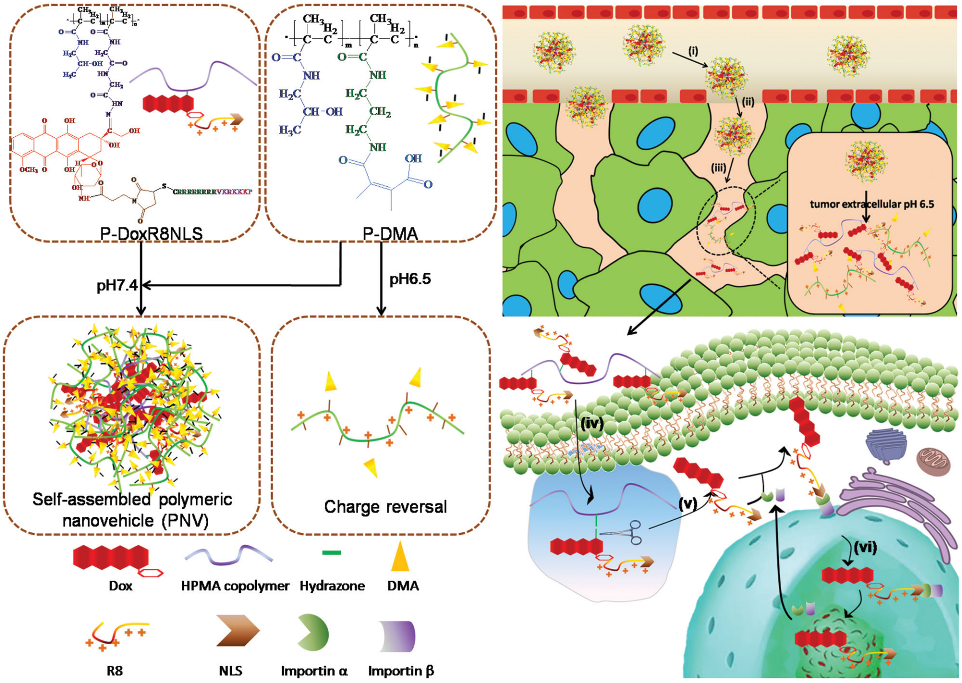

Figure 1. Schematic illustration of a multistage size reduction approach with nuclear homing using HPMA polymeric nanovehicle (PNV). i) Temporary shielding of cationic P-DoxR8NLS in circulation by cross-linking with charge-reversible P-DMA, which is negatively charged at neutral pH to enhance blood retention. ii) Spontaneous self-assembly into PNV through electrostatic attraction, increasing the overall size and therefore eliciting a stronger EPR effect that allows passive accumulation in the tumor. iii) Acidity in the tumor extracellular microenvironment induces charge reversal in P-DMA, causing the self-assembled PNV to collapse into smaller linear copolymers because of electrostatic repulsion. This first-stage size reduction allows the vehicle to penetrate deep into the tissue. iv) Concomitant R8NLS exposure increases vehicle uptake by tumor cells. v) Intracellular release of the IDS when the acidity in the endolysosomal compartment causes hydrolysis of the hydrazone linkage, leading to a second-stage size reduction. vi) Subsequent escape from the endo/lysosome and NLS-assisted nuclear targeting.

achieve long circulation to ensure adequate tumor accumulation. Then, upon charge-reverse of the anionic copolymer due to the first-stage tumor acidity, the PNV would disassemble and shrink into smaller linear conjugates, exposing the R8NLS and thereby increasing diffusion into the tumor interstitial matrix and accelerating cellular uptake. After endocytosis into endolysosome, a second-stage size reduction would occur in response to more acidic endolysosome pH, where the IDS would depart from the copolymer and further reduce its overall size for NLS-assisted nuclear pore complex (NPC) transport.

2. Results and Discussion

As stating earlier, nanovehicles must sequentially decrease in size during the blood-borne delivery to tumor sites, passage through interstitial matrix to contact tumor cells and escaping the endolysosome prior to nucleopore penetration. Coinciding with this “size ladder” requirement, the pH value also declines substantially from blood circulation and normal tissues (pH 7.4) to tumor extracellular environment (pH 6.2–6.9) to intracellular endolysome compartment (pH 4.0–6.0).[14] pH-responsiveness is among most frequently exploited strategies for stimuli-responsive delivery systems. Most recently, dual-pH responsive systems have been developed to trigger charge-reversal and drug release by a few studies.[14] To validate our idea, we used a hydrazone linkage to conjugate an IDS consisting of a doxorubicin (Dox) and R8NLS to the HPMA copolymer backbone (P-DoxR8NLS). This linkage is effectively hydrolyzed at the acidic pH 5 of the endolysosome.[15] In order to avoid premature tissue penetration before tumor arrival and enlarge the vehicle to strengthen the EPR effect, the cationic charge of R8NLS was temporarily masked at pH 7.4 by electrostatic cross-link with anionic 2,3-dimethylmaleic anhydride (DMA) modified HPMA chains (P-DMA) which would undergo charge reversal under tumor acidity pH 6.5.[16] Doxorubicin was used as a model drug here in this first proof-of-principle study, for its intrinsic fluorescence to track the intracellular fate of the IDS and its anticancer therapeutic site being nucleus. Although many reports have validated that Dox which was released in the endosome could promote its nuclei accumulation, Dox, a weak base chemotherapeutic agent, has been previously reported to undergo “ion trapping” in acidic pH where the Dox could be protonated resulting in increased hydrophilicity and weakened transmembrane ability.[17] Compared with free Dox that bypasses the endolysosome and easily enter the cell nucleus, the Dox released in endosome showed a slower and delayed translocation to nucleus, resulting in a sublethal therapeutic concentration and thereby contributing to drug resistance.[17] Conjugating Dox with cell-penetrating peptide would accelerate the endolysosomal escape, but also severely compromises the nuclear accessibility of the parent Dox.[18] To this end, R8NLS peptide was selected as active targeting ligand combining the cell-penetrating properties of R8 with the nuclear homing properties of NLS. Detailed synthesis routes of P-DoxR8NLS and P-DMA were presented in Figure S1 (Supporting Information). As controls to validate the nuclear targeting effect of R8NLS, we prepared HPMA copolymer-Dox conjugates conjugated to either R8 alone (P-DoxR8), NLS alone (P-DoxNLS), or neither peptide (P-Dox). We also synthesized the corresponding Cy5-, Cy5.5-, or FITC-labeled copolymers and prepared PNV for fluorescence resonance energy transfer (FRET) experiments, in vivo imaging and intracellular degradation investigation. Detailed characterizations of all these copolymer conjugates were summarized in Table S1 (Supporting Information), including molecular weight, polydispersity index, Dox loading, peptide content, and fluorescence labeling.

2.1. Characterization, Self-Assembly, and Disassembly of PNV

Initially, negatively charged P-DMA (−26.2 mV) and positively charged P-DoxR8NLS (+18.7 mV) both had a size of ≈10 nm (**Figure 2**a). After cross-linking P-DoxR8NLS with a fourfold molar excess of P-DMA, dynamic light scattering (DLS) of the final structure revealed a distinguished increase in diameter to ≈55 nm, and the overall zeta potential was mildly negative charge (−4.18 mV). These results indicated the successful self-assembly of PNV. Moreover, the particle size and zeta potential of PNV remained hardly changed over 24 h in the presence of 50% fetal bovine serum, indicating no aggregation and relatively good serum stability (Figure S2, Supporting Information). This should be owing to the strengthened structure compactness of PNV via both electrostatic interaction and physical entanglement between oppositely charged P-DMA and P-DoxR8NLS. Also the overall neutralized surface charge of PNV may minimize its aggregation with charged plasma proteins.[19]

Previously, we described a charge shielding/deshielding approach by attaching anionic DMA to cationic amine groups of *N*-3-aminopropylmethacrylamide monomer in HPMA copolymers.[16] The fabricated P-DMA demonstrated selective hydrolysis of DMA under mild acidity of tumor tissues, while remaining stably attached to the copolymers at normal physiology pH. As evident from the zeta potential measurement in Figure 2b, P-DMA underwent a sharp charge conversion within 2 h to become positively charged (from −16.2 to +16.61 mV) at pH 6.5 due to DMA cleavage, while still remain negative charged at pH 7.4 over 8 h. As confirmed in Figure S3 (Supporting Information), the cleavage of DMA in P-DMA rapidly reached ≈50% within 30 min at pH 6.5 and further increased to about 90% with a prolonged incubation time of 2 h, whereas the hydrolysis profile was relatively minor and slow at pH 7.4 reaching a plateau of only 25% DMA release in 4 h. The significantly higher DMA release extent at pH 6.5 than pH 7.4 is consistent with the mild acid-responsive charge-conversional behavior of P-DMA.

Therefore, we expected that at pH 7.4, P-DMA would mask the cationic charge of R8NLS by forming PNV, while at pH 6.5, it would undergo charge reversal and generate strong repulsion to induce PNV disassembly (Figure 2c). To verify this hypothesis, direct morphologies of PNV in response to pH changes were evaluated by transmission electron microscopy (Figure 2d). At pH 7.4, a spherical shape of PNV was observed with compact structure and symmetrical size, which agreed well with the size measured by DLS. By comparison, the PNV appeared to disassemble, and exhibited irregular and lose

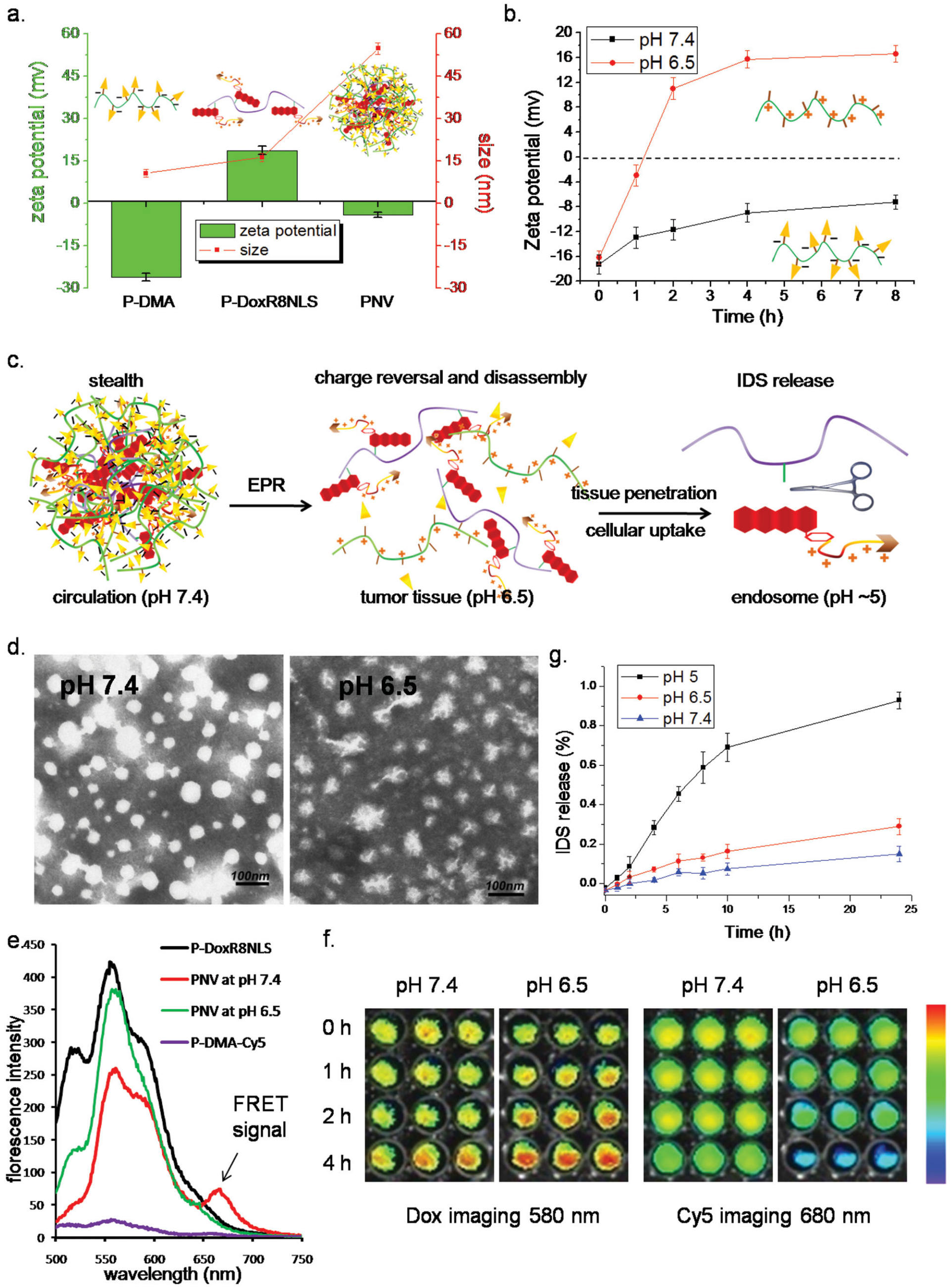

Figure 2. Characterization, self-assembly, and disassembly of PNV. a) Size and zeta potential of P-DMA and P-DoxR8NLS conjugates before and after cross-linking in aqueous solution. b) Zeta potential variation of P-DMA as a function of incubation time at pH 7.4 or 6.5. c) Schematic mechanism of multistage size-reduced PNV. d) Transmission electron images of PNV incubated at pH 7.4 or 6.5 for 2 h. e) Fluorescence resonance energy transfer (FRET) spectra of PNV acquired at 2 h after incubation at pH 7.4 or 6.5. f) Dual emission images of Cy5-modified and Dox-loaded PNV incubated at environmental pH for 0, 1, 2, and 4 h. g) Time-dependent cumulative release of the IDS from P-DoxR8NLS conjugates at pH 7.4, pH 6.5, and pH 5.

morphology at pH 6.5 that mimics tumor tissue milieu, suggestive of pH-induced disintegration.

To further confirm PNV stability at pH 7.4 and disassembly at pH 6.5, FRET was used to analyze the spatial interaction between P-DoxR8NLS and P-DMA-Cy5 at the two pH conditions. In these experiments, FRET was possible only when the excited donor chromophore (Dox) was sufficiently close to the acceptor chromophore (Cy5), giving rise to a peak around 675 nm.[20] No FRET peak was observed when solutions of P-DoxR8NLS alone or P-DMA-Cy5 alone were irradiated at the Dox excitation wavelength of 480 nm (Figure 2e). When PNV was incubated at pH 7.4, FRET signal was observed together with a reduction in Dox fluorescence intensity, clearly indicating an energy transfer. Interestingly, this FRET signal disappeared when PNV was incubated at pH 6.5. The charge repulsion, induced by the charge switch of P-DMA, should be responsible

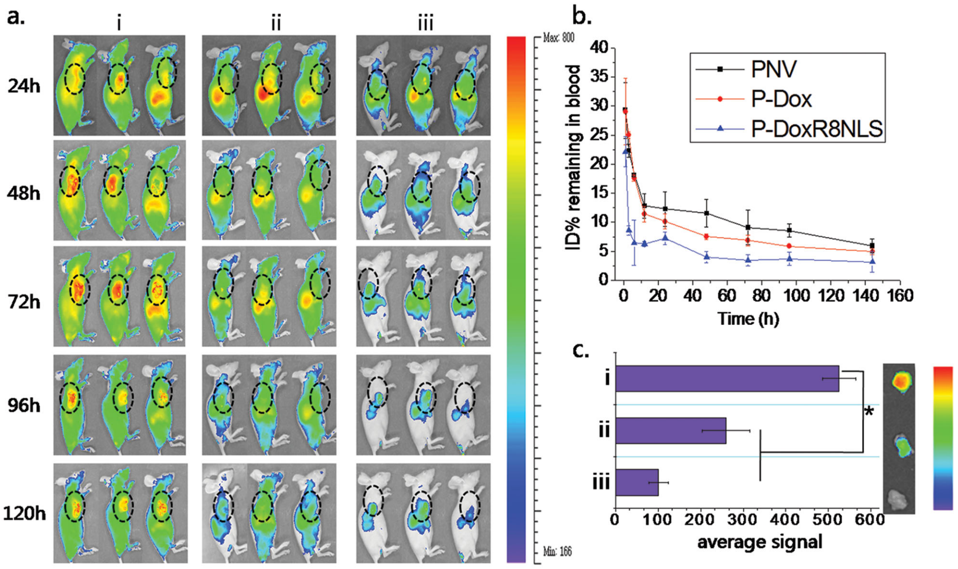

Figure 3. a) Real-time fluorescence imaging of mice treated with of Cy5.5-labeled (i) PNV, (ii) unmodified P-Dox, and (iii) unprotected P-DoxR8NLS at 24, 48, 72, 96, and 120 h after intravenous injection. Fluorescence intensities were normalized to the same scale. Black circles indicate the tumor. b) Pharmacokinetic profiles of Cy5.5-labeled PNV, P-Dox, and P-DoxR8NLS in BALB/c mice after intravenous injection. At different time points, blood samples were taken; residual blood fluorescence intensity is presented as %ID (injected dose) remaining in total blood. c) Imaging of the excised tumors at 48 h postinjection (*$p < 0.05$).

for this FRET off. In this situation, Dox and Cy5 were no longer accessible for energy transfer due to the PNV disassembly. Further insight into the arrangement of Dox and Cy5 in PNV was obtained by analyzing the dual-emission images of PNV at the two pH values (Figure 2f). Both Dox and Cy5 fluorescence showed only modest changes over time at pH 7.4, reflecting relative stability under physiological environment. In contrast, Cy5 fluorescence gradually diminished and Dox fluorescence gradually increased at pH 6.5, indicating eventual separation of the two components over time.

Considering the nuclear pore limit for exogenous macromolecules, the P-DoxR8NLS conjugates (≈39 kDa, Table S1, Supporting Information) released from the PNV in response to first-stage size reduction may still be too large to cross the nuclear membrane. Therefore, a further cargo size decrease would be imperative. In the present study, the hydrazone bonds were selected as the spacer between macromolecular HPMA copolymer backbone and small molecular doxorubicin-peptide derivative IDS (≈2.4 kDa), since this linkage would become increasingly labile at more acidic endolysosomal pH (pH ≈ 5).[15,16] As shown in Figure 2g, only 24.4% and 14.9% DOX were released at pH 6.5 and pH 7.4, respectively. The release rate at pH 6.5 is slightly higher than at pH 7.4, but still remains at a significantly low level compared with the release rate at pH 5, indicating the premature hydrolysis of hydrazone linkage at tumor tissue could be efficiently reduced. These results were consistent with previous reports from our group[16] and other groups.[14] In contrast, IDS release from P-DoxR8NLS was significantly faster at pH 5 than at pH 7.4 or 6.5, reaching 92.8% after 24 h incubation due to cleavage of the hydrazone linkage. This confirms the second-stage size reduction from linear conjugate to smaller IDS in a pH-dependent manner.

2.2. Increased Body Circulation and Tumor Accumulation before First-Stage Size Reduction

To determine whether the combination of nanovehicle size expansion and charge masking of R8NLS could improve PNV biodistribution, we compared the in vivo fate of intravenously administered PNV, P-Dox, and unprotected P-DoxR8NLS in real time (**Figure** 3a). After normalizing the fluorescence intensity to the same scale, cationic P-DoxR8NLS conjugate alone was rapidly eliminated from the body, as evidenced by the ever-decreasing intensity of overall weak body fluorescence since the first day after injection. The lack of specificity of cationic R8NLS and higher recognition by MPS in circulation might presumably account for this quick body clearance, which was supported by numerous reports on the restriction of CPP in vivo application[12] and again reinforced the necessity for averting premature CPP penetration. PNV, in contrast, showed a sustained systemic distribution throughout the 120 h study period, reflecting adequate blood residence time and confirming its capability to minimize nonspecific binding by shielding CPP charge. Moreover, PNV also exhibited substantially longer systemic persistence than linear P-Dox conjugates, although both samples had nearly neutral zeta potentials. This difference was particularly pronounced between 48 and 120 h, as confirmed in the pharmacokinetics study (Figure 3b). Their major discrepancy in size may be responsible for this observation, since the larger sized PNV (≈55 nm) over linear P-Dox (≈10 nm) and renal threshold was less prone to renal excretion through glomerular filtration.[21] This result is in agreement with our previous findings that increasing the size of HPMA copolymers to micelles led to extended circulation half-life.[15]

Increasing nanocarrier persistence in circulation increases its opportunities to extravasate into tumor tissue by the EPR effect and should thereby increase tumor accumulation. Consistent with this, we observed much greater tumor accumulation for PNV, which peaked at 48 h and lasted for at least 120 h, than for unmodified P-Dox and unprotected P-DoxR8NLS conjugates, which were barely detectable in tumors even at 48 h (Figure 3a). As shown in Figure 3c, the fluorescence intensity of tumor tissue of PNV after 48 h injection was twofold greater than the linear P-Dox and almost fivefold higher than the charge-unmasking P-DoxR8NLS. The more pronounced EPR effect due to the enlarged size and neutralized charge of PNV could result in its greater tumor accumulation. Therefore, a prolonged circulation half-life and enhanced tumor accumulation in vivo could be achieved by the combination of larger size and R8NLS-masking during the intact stage of PNV.

2.3. Enhanced Tumor Penetration and Cell Uptake after First-Stage Size Reduction

After reaching the tumors, another level of barrier that PNV had to face, during transport through tumor interstitial space to reach targeted cells, was imposed by the dense and viscous nature of the extracellular matrix (ECM).[1] Some recent studies suggest that larger nanoparticles (≈100 nm) are mostly trapped at the tumor periphery, whereas smaller ones (≈10 nm) were more capable of tumor penetration.[5,6b] In other words, the large size that endowed the nanovehicles with stronger EPR effect also imposes greater diffusion limitations in ECM. However, despite this size discrimination, the strong and sustained retention of PNV inside tumors over 5 d in our experiments suggested deep tissue penetration. Thus, it was reasonable to anticipate that tumoral acidity-driven transition from larger PNV to shrinking linear copolymers would eventually increases tissue infiltration. To verify this hypothesis, the tumor blood vessels were labeled with CD31 biomarkers and the intratumoral distribution of systemically administered PNV were evaluated (**Figure 4**a). As expected, the larger size of PNV did not hinder its tumor penetration and it even spread more widely around vessels by the virtue of the subsequently reduced size after its greater EPR effect. The inferior tumor diffusion activity of other groups could stem from the restricted vascular extravasation due to less blood residence time and tumor accumulation.

To further demonstrate that first-stage size reduction triggered by tumor extracellular pH is crucial for tumor penetration, diffusion of PNV into tumors was examined ex vivo by exposing excised cancer tissue to PNV in cell medium at both pH 7.4 and 6.5, followed by imaging of the surface and interior of cryostat-sectioned tissues (Figure 4b). Notably, PNV at pH 7.4 showed minimal penetration, with Dox fluorescence concentrated mostly along the tumor edge. At pH 6.5, in contrast, Dox fluorescence within the tumor was strong and homogeneous, probably as a result of PNV disassembly. This was similar to several other size-shrinking strategies that release small and cationic particles or dendrimers to realize enhanced tumor penetration.[22] In another experiment, a 3D tumor spheroid model, which mimics solid tumors, was employed to predict the tumor penetration ability (Figure 4c). Consistent with above results, dramatically higher spheroid penetration was attained by the PNV incubated at pH 6.5 than pH 7.4.

After gaining access to the cells, additional advantage of the first-stage size reduction would be the exposure of cationic R8NLS ligand to promote endocytosis. Therefore, we next compared the uptake of PNV by HeLa cells at pH 6.5 and 7.4 using confocal microscopy (**Figure 5**). Only marginal uptake of Dox occurred at pH 7.4, whereas incubating PNV at pH 6.5 for 2 h delivered significantly more Dox into cells. Also flow cytometry results further confirmed this pH-dependent cellular internalization. In addition, the endocytosed carriers at pH 6.5 were almost located in lysosomes, a prerequisite place for the subsequent separation of IDS from HPMA copolymer backbone.

2.4. Efficient Nuclear Targeting after Second-Stage Size Reduction

Following endocytosis, the nuclear envelope presents the last but most formidable hurdle for nuclear delivery. Cell nucleus is separated from the cytoplasm by nuclear envelope with a double membrane structure, and the access to the interior of nucleus is governed by the NPC with an opening of ≈9 nm in functional diameter.[23] Only conjugates less than 15 kDa in molecular weights are able to go through the NPC.[9] Since the NPC confers the only available passages for material exchange, passing through it requires sufficiently small size and an active ligand targeting it.[7a] Mostly, nuclear-homing ligands such as TAT peptides were directly conjugated onto the backbones of drug-loaded carriers. However, the nanocarrier's size may either be too small to elicit a strong EPR effect or too large to cross the NPC, thus offsetting active targeting. Therefore, we introduced functional IDS onto the HPMA conjugates backbone (P-DoxR8NLS) via a hydrazone linkage susceptible to hydrolysis at endolysosomal pH. The scenario in the present design is that after HPMA copolymer (≈39 kDa) finished its task as drug carrier, the nucleus-targeting IDS (≈2.4 kDa) would depart to reduce its overall size for NPC transport.

To demonstrate the intracellular second-stage size reduction in response to endolysosomal pH, dual-labeled P(FITC)-DoxR8NLS was used with FITC as the backbone tag and Dox as the model drug. LysoTracker Blue DND-22, a blue fluorescent dye that stains acidic compartments in live cells, was used to mark the endolysosomal organelles. As observed in **Figure 6**, the internalized P(FITC)-DoxR8NLS was initially found to remain sequestered within the endolysosomal system after 2 h incubation. This indicated that like most of the lysosomotropic macromolecules, P(FITC)-DoxR8NLS copolymers were internalized via the endocytosis pathway into endolysosome, where IDS could be released. Whereas, over time (4 h), more Dox florescence appeared outside endolysosomes and located at a distance from the FITC florescence which was still trapped in the endo/lysosome, suggesting the detachment of IDS from HPMA copolymer backbone. The successful endolysosomal escape of IDS after second-stage decrease of cargo size was also accompanied by gradually increasing amount of Dox florescence inside nuclear. To validate that the cleavage of IDS from HPMA copolymer backbone contributed to its nuclei entry, cells were exposed to 50×10^{-3} M NH_4Cl, which could induce blockage of the early-to-late endosome acidification progression.[24] As evidenced by the NH_4Cl pretreatment, the florescence intensity

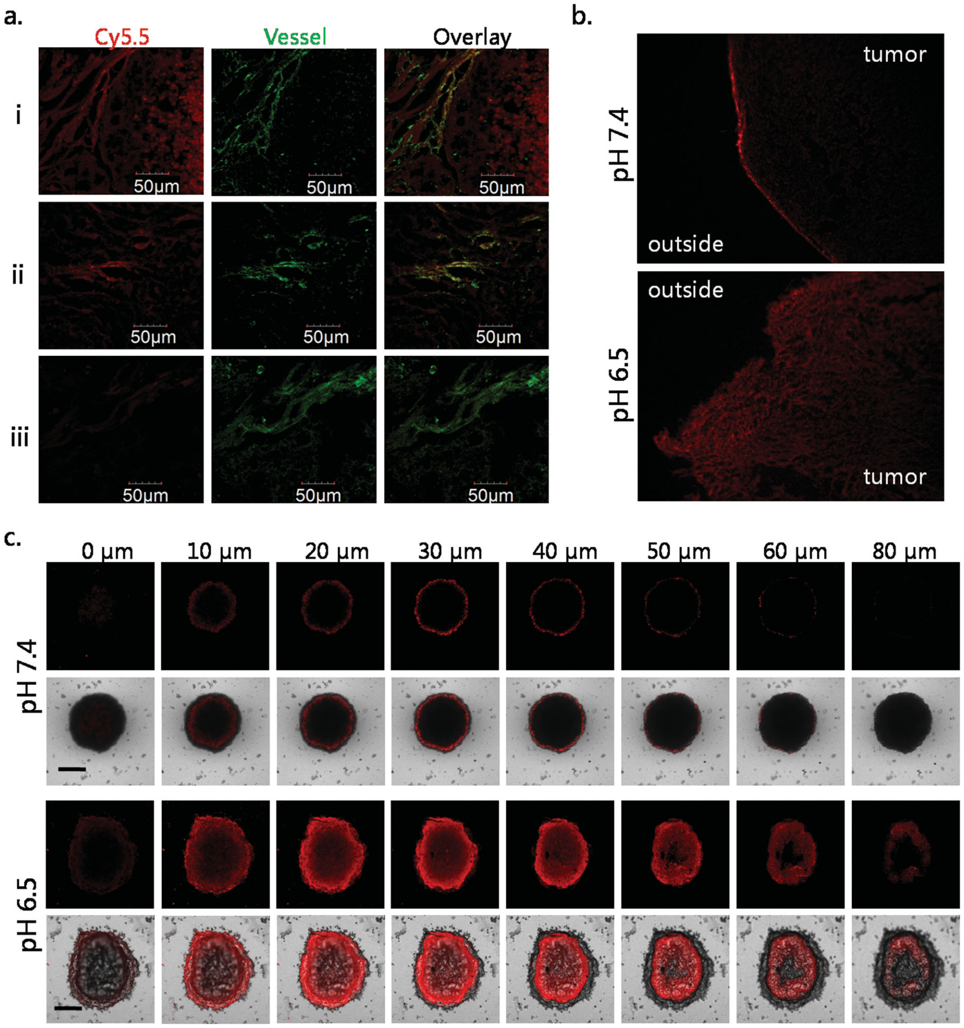

Figure 4. a) Frozen sections of tumors were removed at 48 h after treatment with Cy5.5-modified (i) PNV, (ii) P-Dox, and (iii) P-DoxR8NLS (red signal) and then stained with FITC-tagged CD31 antibody to label tumor vessels (green signal). b) HeLa tumors were cultured for 24 h in the presence of PNV in medium adjusted to pH 7.4 or 6.5. Tumor sections (20 μm thick) were harvested by cryostat and imaged to show the Dox (red signal) distribution on the edge and inside area of tumor sections. c) Representative confocal microscopy images of pH-dependent penetration of PNV into HeLa tumor spheroids to different depths. Scale bar: 200 μm.

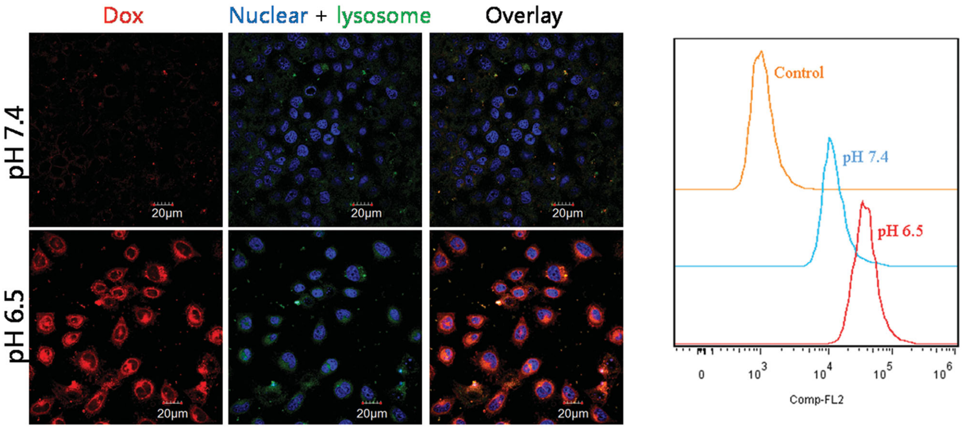

Figure 5. Tumor pH-selective cell uptake of PNV after incubation for 2 h. Yellow color denotes the overlay of Dox fluorescence (red) and endolysosome staining (green), while blue shows DAPI staining of nuclei.

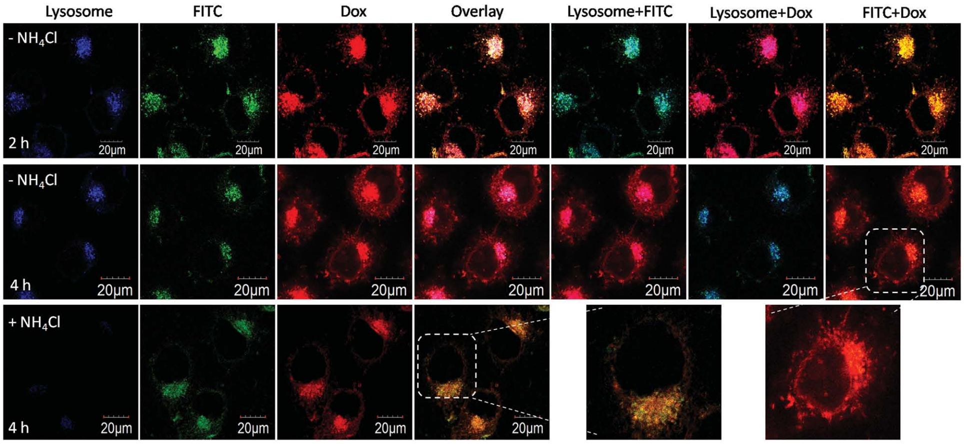

Figure 6. Intracellular degradation of P(FITC)-DoxR8NLS in endolysosomes with or without NH_4Cl pretreatment. Red: Dox fluorescence. Green: FITC fluorescence from polymer backbone. Blue: endolysosomal staining.

of the pH-sensitive marker LysoTracker Blue DND-22 decreased dramatically. Without the endolysosomal pH responsiveness, the majority of FITC fluorescence from HPMA backbone was dominantly overlaid with the Dox florescence at 4 h, indicating the undetachment of IDS. This also severely limited the presence of IDS inside nuclear, which was in contrast to the group without NH_4Cl pretreatment.

Besides decreased cargo size, R8NLS-mediation might also partially determine successful nuclear accumulation. To clarify the important role of R8NLS, the in vitro internalization efficiency was next evaluated by cellular uptake study (**Figure 7**a and Figure S4, Supporting Information). Uptake was greatest for P-DoxR8NLS, followed by P-DoxR8 and P-DoxNLS, while much weaker fluorescence from P-Dox was observed due to its intrinsically poor membrane affinity.[25] To reliably distinguish the conjugates that actually entered the cell from those just adsorbed on the cell surface, we compared flow cytometry results before and after quenching extracellular Dox fluorescence using trypan blue (TB).[26] Interestingly, P-DoxNLS displayed the greatest reduction extends (40%) after TB quenching, indicating cell surface adhesion driven by cationic NLS did not exert significant effect on cell internalization. Similarly, there were corroborating reports of major impediment for NLS utilization being its inability to cross cell membrane.[27] By comparison, P-DoxR8 retained the most percentage of remaining fluorescence (only 16% reduction in fluorescence after TB quenching), benefiting from the efficient penetration of R8. Notably, P-DoxR8 even exhibited comparable intracellular concentration as P-DoxR8NLS (after TB treatment). Regarding R8NLS-mediated cell penetration, our results suggest that NLS

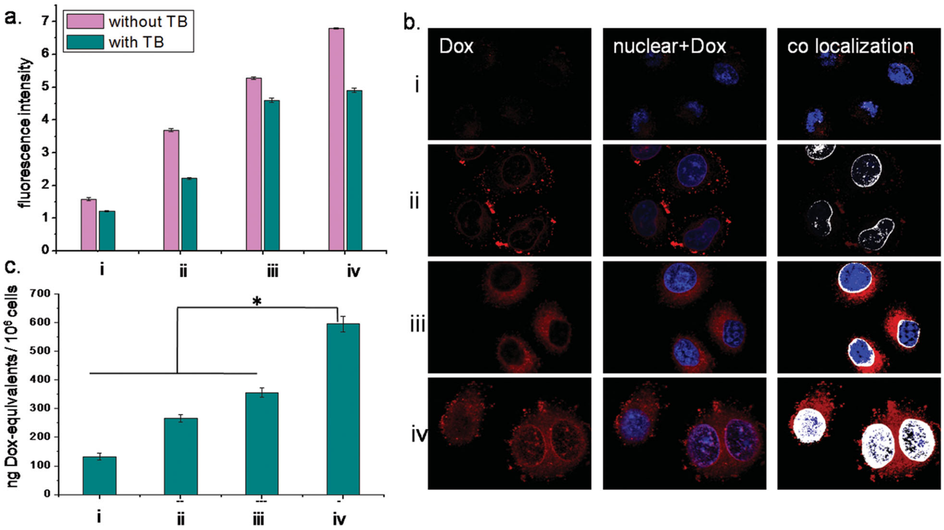

Figure 7. a) Cellular uptake of (i) P-Dox, (ii) P-DoxNLS, (iii) P-DoxR8, and (iv) P-DoxR8NLS at an equivalent Dox dose of 10 μg mL^{-1} incubated for 4 h before and after trypan blue (TB) quenching. b) Nuclear targeting of Dox-loaded conjugates at an equivalent Dox dose of 10 μg mL^{-1} after 4 h incubation and subcellular organelle staining. White indicates the colocalization of Dox (red) and nuclei (blue) analyzed using ImageJ software. c) Quantitative measurement of nuclear Dox content after incubating HeLa cells for 4 h with Dox-loaded conjugates at equivalent Dox dose of 10 μg mL^{-1} ($n = 3$, $*p < 0.05$).

contributed negligibly, while it was R8 that played a dominant role in efficient cell internalization.

We then investigated the nuclear targeting ability of these conjugates using confocal microscopy (Figure 7b). Barely detectable fluorescence of P-Dox was observed inside cells. In accordance with above cellular uptake experiments, P-DoxNLS was associated mostly with the cell membrane and only a small proportion of Dox entered the nucleus, which again highlighted the challenges that NLS on its own is ineffective at targeting the drug to the nucleus because of poor internalization efficiency. As for P-DoxR8, despite its extensive entry into cells, it showed strong fluorescence in the perinuclear region with limited presence inside the nucleus, indicating that R8 was more involved in cellular uptake rather than nuclear transfer, which was consistent with the research that distribution of Dox-CPP conjugation was mainly constrained in cytoplasm.[18] In contrast, owing to the active targeting to NPC by NLS after R8-mediated endocytosis, an overwhelmingly stronger Dox fluorescence from P-DoxR8NLS was overlaid with nucleus, suggesting the fusion of NLS conquered the nuclear inaccessibility of R8. As Dox binding to DNA has been reported to quench its fluorescence intensity,[28] quantitative measurement of Dox content by extracting it from nuclear was performed to more precisely evaluate the nuclear distributions of these conjugates (Figure 7c). Again, P-DoxR8NLS achieved the highest nuclear accumulation, ≈1.8-fold higher than P-DoxR8, 2.2 times higher than P-DoxNLS, and nearly 4.5 times higher than P-Dox. Collectively, when integrated together, R8 primarily engaged in cellular internalization and NLS having major contributions in nuclear localization highly complemented to each other, collaboratively making the tandem R8NLS an effective nuclear targeting cell penetrating peptide.

As expected, P-DoxR8NLS also triggered the most potent cell killing activity over other conjugates (Figure S5, Supporting Information), owing to its more efficient nuclear targeting. As free Dox interacts with nuclear DNA by intercalation and inhibition of macromolecular biosynthesis, the CPP modification may exhibit steric hindrance and imposes greater hurdle for Dox-CPP to interact with DNA, thereby comprising the potency of Dox. Therefore, in a purified, biochemical form, a less cell killing potency of R8NLS-Dox than free Dox alone can be anticipated. However, this shortfall could be reversed when conjugating the CPP-Dox onto the HPMA copolymers. All ligand modified conjugates showed higher cytotoxicity than unmodified HPMA-Dox, indicating that the ligand potentiates the potency of Dox conjugated to the HPMA copolymers since the improved drug uptake could counteract the possible decreases in drug activity that resulted from ligand–Dox conjugation.[29] It should be noted that the peptide ligand itself does not contribute to the cytotoxicity (Figure S5a, Supporting Information). Regarding the ligand type, P-DoxR8NLS exhibited a superior toxicity over P-DoxR8 and P-DoxNLS (Figure S5b, Supporting Information), due to the synergetic effect of R8NLS to combine the membrane penetrating abilities endowed by R8 and nuclear targeting competence inherited from NLS. It should be noted that Dox coupled to CPPs displayed in most cases cytoplasmic distribution, which is in contrast to the free Dox that localizes mainly in nucleus, probably as a result of the modification made to the Dox structure that impedes its nuclear interaction.[18] As revalidated in our study, P-DoxR8 showed enhanced cell internalization but limited nuclear uptake, indicating that conjugation of R8 greatly impaired the nucleus-tropic trait of Dox. By adding an NLS to the octaarginines peptide sequence, enhanced nuclear targeting and therapeutic efficacy was obtained by the P-DoxR8NLS, implying that the nuclear accumulation was due to the NLS targeting rather than the Dox tendency. Combined with the distinctly different intracellular distribution pattern with or without NH_4Cl pretreatment, R8NLS ligand and decreased cargo size are intracellularly dispensable for nuclear entry. Our findings could serve as a proof-of-concept study of utilizing intracellular detachable subgroup with small enough size and nuclear-homing ligand to achieve efficient nuclear targeting. Such nuclear targeting approach might also show its feasibility and potential for delivering other nuclear-toxin drugs, e.g., DNA.

2.5. Nuclear Localization and Anticancer Activity of PNV In Vitro and In Vivo

To further assess the nuclear targeting of PNV, intracellular distribution in vitro was visualized by Z-stack confocal images (**Figure 8**a). Similar with unmodified P-Dox conjugates, barely visible Dox fluorescence was overlaid with the nuclear for the PNV incubated at pH 7.4. Meanwhile, a distinctly different nuclear distribution pattern was produced by the PNV at pH 6.5, where abundant amount of Dox finally reside in nuclear. More excitingly, in an in vivo xenograft tumor model, intravenously administered PNV led to a much greater proportion of red Dox fluorescence that colocalized with 4′,6-diamidino-2-phenylindole (DAPI)-stained nuclear than administering P-Dox did, suggesting that PNV is more effective at delivering Dox to tumor cell nuclei in vivo (Figure 8b and Figure S6, Supporting Information).

To further verify therapeutic efficacy in vivo, we evaluated the ability of PNV and conjugates to inhibit HeLa tumor growth in nude mice (Figure 8c). The four treatments suppressed tumor growth to varying extents, with the lowest inhibition (50%) shown by free Dox, compared with 61% for P-Dox, emphasizing the importance of the EPR effect for targeted delivery. P-DoxR8NLS caused only 54% inhibition, which provides additional evidence for in vivo restriction of cationic CPP. On the other hand, PNV achieved the highest rate of tumor growth suppression (75%), and showed no apparent body weight loss (Figure S7, Supporting Information). The survival curves of HeLa tumor-bearing mice of each group after receiving different treatments (Figure S8, Supporting Information) also indicate that the PNV can improve the drug therapeutic index and prolong the survival of tumor-bearing mice. This dramatic therapeutic improvement could be due to the PNV's capability to conquer multiple barriers for systemic nuclear delivery by covering several essential attributes including long blood circulation, adequate tumor accumulation, deep tissue penetration, efficient cell uptake, rapid endolysosomal escape, and ultimately nuclear transport. We attributed this to two key features of PNV: sequential size reduction and on-demand R8NLS exposure.

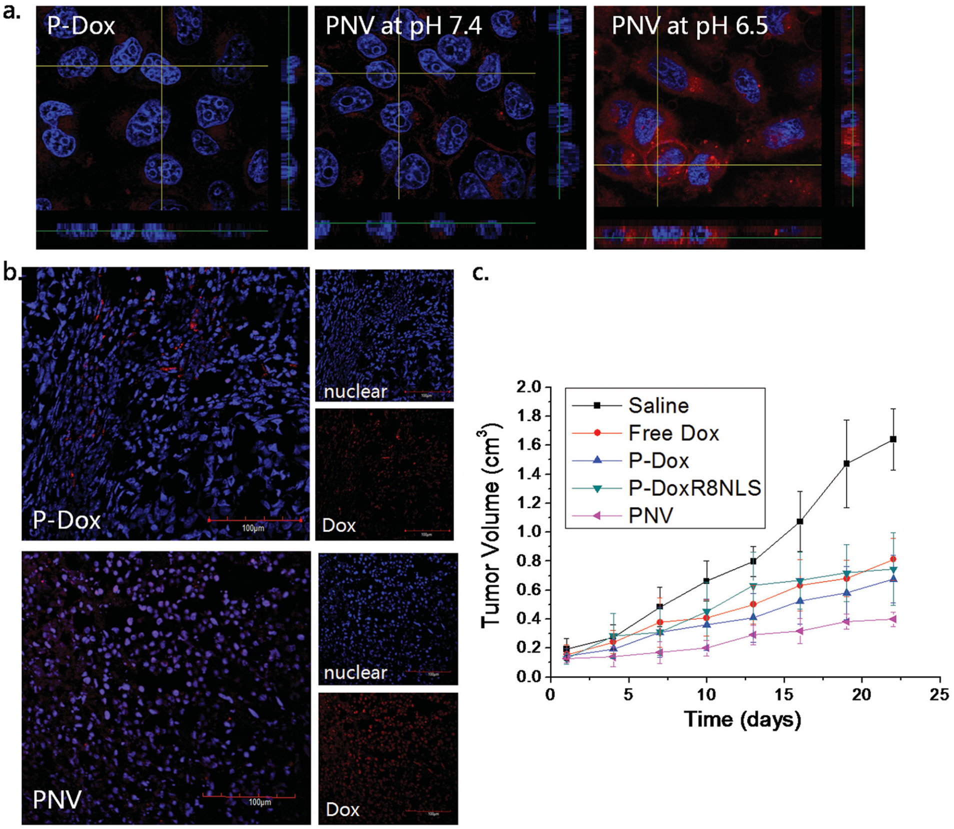

Figure 8. a) Z-stack images of PNV nuclear uptake in HeLa cells after 4 h incubation. Red: Dox fluorescence from the PNV or unmodified P-Dox. Blue: DAPI-stained nuclei. b) In vivo subcellular distribution of P-Dox and PNV within the cryostat sections of central tumor tissues from mice that received intravenous injections of equal doses of Dox. Red: Dox fluorescence from the conjugates or PNV. Blue: DAPI-stained nuclei. c) Tumor growth curves from HeLa tumor-bearing nude mice given different Dox-loaded formulations ($n = 5$).

3. Conclusion

A multistage stimuli-responsive PNV with sequential size reduction and on-demand R8NLS exposure was prepared by cross-linking cationic P-DoxR8NLS and anionic P-DMA to allow nuclear delivery of systemically administered drugs. The nanosystem underwent a sequential transition from originally large, self-assembly PNV (≈55 nm) to smaller linear conjugates (≈10 nm/39 kDa) to further decreased IDS (≈2.4 kDa) in response to both tumor extracellular and endolysosomal acidic stimuli. At the circulation level, the large, neutrally charged, self-assembled PNV showed favorable pharmacokinetics and preferential tumor accumulation. Upon arriving at the tumor site, the first-stage size reduction was triggered by extracellular milieu-actuated PNV disintegration, thus facilitating the extravasation from vasculature and diffusion in the tumor extracellular space. At the cellular level, the exposure of cationic cell penetrating peptide R8NLS also accelerated cell internalization. At the intracellular level, in response to the endolysosomal cleavage of hydrazone spacer, the second-stage size reduction initiates with the departure of IDS from HPMA copolymer backbone. This further decreased cargo size guaranteed the successful nuclear entry via NLS-mediation and exhibited 4.5-fold higher nuclear accumulation than the HPMA-Dox. Ultimately, PNV showed good nuclear targeting in vivo, and they inhibited tumor growth by 75%.

4. Experimental Section

Materials: Doxorubicin hydrochloride (DOX·HCl) was purchased from Dalian Meilun Biotech Co., Ltd. (Dalian, China). Cyanine 5 NHS ester (Cy5-NHS) and Cyanine 5.5 NHS ester (Cy5.5-NHS) were purchased from Lumiprobe (USA). A series of functional monomers including HPMA, *N*-methacryloylglycylglycyl-hydrazide-doxorubicin (MA-GG-NHN = DOX), Cy5/Cy5.5 methacrylamide monomer (MA-Cy5/Cy5.5), and *N*-methacryloyl-aminopropyl-fluorescein-5-isothiocyanate (MA-AP-FITC) were synthesized in our laboratory as described. *N*-3-aminopropylmethacrylamide hydrochloride (APMA) was purchased from PolyScience. DMA was obtained from Acros Organics. *N*-Succinimidyl 3-maleimidopropionate (SMP) was purchased from Haofan Biomatrix Co. Ltd. (Suzhou, China). R8 peptide (CRRRRRRRR), NLS peptide (CVKRKKKP), and R8NLS peptide (CRRRRRRRRVKRKKKP) were synthesized by Kaijie Biopharm Co. Ltd. (Sichuan, China). 3-(4,5-Dimethyl-2-tetrazolyl)-2, 5-diphenyl-2H tetrazolium bromide (MTT), and DAPI were purchased from Sigma-Aldrich (St. Louis, MO, USA). Lysotracker Green/Blue was purchased from Invitrogen (Carlsbad, CA, USA). Rat anti-CD31 antibody was purchased from BD Bioscience (San Diego, USA) and goat antimouse fluorescein-conjugated immunoglobulin G was obtained from Beijing Biosynthesis Biotechnology Co. Ltd. (Beijing, China). All the other chemicals were of analytical grade.

Synthesis and Characterization of Various Conjugates Based on HPMA Copolymers: The synthesis routes of DMA-modified charge-reversible conjugates (P-DMA) and IDS containing HPMA copolymer conjugates (P-DoxR8NLS) were presented in Figure S1 (Supporting Information). P-DMA was synthesized in two steps, as reported.[16] Briefly, positively charged amine groups containing polymer precursor (APMA copolymer) were prepared by radical solution copolymerization in methanol (AIBN, 2 wt%; monomer concentration, 12.5 wt%; molar ratio of HPMA/APMA,60:40). Copolymerization was carried out in sealed ampoules under nitrogen at 50 °C for 24 h. The copolymer was isolated from polymerization mixture by precipitation into diethyl ether, followed by dialysis against distilled water for 24 h and freeze-drying. Then APMA copolymer was dissolved in sodium bicarbonate buffer (0.1 M, pH 8.5), and DMA (3 molar equivalents to APMA monomer) was slowly added. With the addition of DMA, the pH decreased rapidly and was maintained in the range of 8.0–8.5 by simultaneous addition of 0.2 N NaOH. After all DMA was added, the solution was stirred for 4 h, and then was dialyzed against sodium bicarbonate buffer (0.1 M, pH 8.5) for 2 d and lyophilized to obtain the DMA-protected conjugates P-DMA. P-DoxR8NLS was synthesized in three steps. First, P-Dox were prepared by radical solution polymerization in methanol (AIBN, 2 wt%; monomer concentration, 12.5 wt%; molar ratio of HPMA/MA-GG-NHN = Dox, 92.5:7.5) and purified as described above. Then the copolymer, SMP and triethylamine (TEA) were dissolved in dimethylformamide (DMF) and stirred for 4 h at room temperature.[29] The reaction solution was precipitated using cold anhydrous diethyl ether, then vacuum-dried. Finally, R8NLS peptide was attached to the Dox molecule to form a P-Dox copolymer intermediate via the highly specific reaction between the maleimide and thiol groups. Briefly, R8NLS peptide and the conjugates were dissolved in phosphate-buffered saline (PBS, pH 7.0). Argon was bubbled through the solution to remove oxygen. Then, the reaction was allowed to proceed overnight at room temperature. The reaction mixture was purified in deionized water for at least 48 h using dialysis tubing with a 5 kDa molecular weight cutoff, and then freeze-dried to obtain the final product P-DoxR8NLS. P-DoxR8 and P-DoxNLS conjugates were prepared by the same procedure. For FRET measurements, in vivo imaging and dual-fluorescence labeling, the corresponding Cy5- or Cy5.5-labeled conjugates and FITC-labeled conjugates were synthesized by similar methods, except that the MA-Cy5/Cy5.5 monomer and MA-AP-FITC monomer replaced 2 mol% of HPMA monomer in the random radical copolymerization. The molecular weight and polydispersity index (PDI) of the conjugates were estimated by size exclusion chromatography on a Superose 200 10/300GL analytical column (Amersham Biosciences, NJ) calibrated with poly (HPMA) fractions using a fast protein liquid chromatography system (AKTA FPLC; Amersham Biosciences, NJ, USA). The content of Dox in copolymers was determined in deionized water using vis-spectrophotometry at an absorbance at 481 nm ($\varepsilon_{481\ \text{nm}}$ = 9860 M^{-1} cm^{-1}). The fluorescence intensity of Cy5-/Cy5.5-labeled copolymers was measured by fluorescence spectrophotometry (RF-5301PC, Shimadzu) at an excitation wavelength of 650/674 nm and an emission wavelength of 680/694 nm. The peptide contents of the conjugates were determined by amino acid analysis (Commonwealth Biotech, VA, USA). Detail characterization of each conjugate is provided in the Supporting Information.

Preparation and Characterization of PNV: PNV was prepared by cross-linking P-DoxR8NLS and P-DMA in a 1:4 molar ratio in PBS. The mixtures were vortexed and stirred at room temperature for 10 min. Mean sizes and zeta potential of P-DMA, P-DoxR8NLS, and PNV were measured on a Zetasizer Nano ZS90 (Malvern Instruments, UK). To demonstrate the serum stability of PNV, particle size and zeta potential were monitored in the presence of 50% fetal bovine serum. PNV morphology was analyzed using transmission electron microscopy (Hitachi H-600, Tokyo, Japan). PNV was incubated for 2 h in buffer solutions at pH 7.4 or 6.5, then a drop of these solutions was deposited on the surface of a carbon-coated copper grid and stained with 2% (w/v) phosphotungstic acid for 30 s. For FRET measurement, the emission spectra of PNV (mixture of P-DoxR8NLS and P-DMA-Cy5) were determined at pH 7.4 and 6.5 using fluorescence spectrometer.[20] The donor (Dox) was excited at 485 nm and the emission spectra of the donor/acceptor were recorded at all wavelengths simultaneously. Control spectra were also obtained using P-DoxR8NLS or P-DMA-Cy5 on their own. Dual-emission images of fluorescent PNV at different incubation times and pH values were acquired using Bio-Real Quick View 3000 in vivo imaging system (Geneway International, Austria). PNV solutions (1 mg mL^{-1}, 200 mL per well) were loaded into a 96-well plate, irradiated at a wavelength of 480 nm and imaged with bandpass emission filters to obtain unmerged images of Dox fluorescence (580 nm) and Cy5 fluorescence (680 nm). For the measurement of IDS release, 300 μL of P-DoxR8NLS conjugates (equivalent Dox concentration: 10 mg mL^{-1}) was dialyzed against 15 mL of PBS buffer at pH 6.5 or 7.4 or against 15 mL of acetate buffer at pH 5 in dialysis tubing with a 2 kDa molecular weight cutoff. At predetermined time points, 100 μL of external buffer was collected and replaced with fresh buffer. Dox concentration was determined using a Varioskan Flash (Thermo Fisher Scientific, MA, USA) with excitation at 485 nm and emission at 590 nm.

In Vivo Imaging and Biodistribution Analysis: HeLa tumor-bearing mice were randomly divided into three groups (n = 3 per group), and intravenously injected with Cy5.5-labeled PNV, P-Dox, or P-DoxR8NLS (0.04 μmol Cy5.5 per mouse). Real-time images of anesthetized mice were obtained at 1, 2, 3, 4, and 5 d postinjection using the Bio-Real Quick View 3000 in vivo imaging system. To compare the tumor distributions of the above samples, mice were sacrificed at 48 h postinjection. Tumors were dissected, washed with normal saline, and imaged immediately using the in vivo imaging system. All animals used above received care in compliance with the guidelines outlined in the Guide for the Care and Use of Laboratory Animals and all procedures were approved by Sichuan University Animal Care and Use Committee.

Pharmacokinetics Study: For the pharmacokinetic study, healthy BALB/c mice were intravenously injected with Cy5.5-labeled PNV, P-Dox, or P-DoxR8NLS (0.04 mol Cy5.5 per mouse). At each time points, blood samples (10 μL) were taken from the orbital, and the fluorescence intensity of each sample was measured with a Varioskan Flash (excitation at 680 nm and emission at 694 nm).

Penetration Assay: To study the tumor vascular permeability, the mice were sacrificed 48 h after administration and the harvested tumors were frozen and cut into 10 μm slices and stained with DAPI (5 μg mL^{-1}) for 5 min. Tumor slices were fixed in 4% paraformaldehyde for 20 min, blocked with 10% BSA for 1 h, and incubated with rat anti-CD31 antibody (1:50, 550274, BD Biosciences, San Diego) overnight at 4 °C. Sections were rinsed in PBS and incubated with a FITC-conjugated goat antirat IgG secondary antibody (1:100, Bioss, Beijing) for 1 h, then washed, and sealed with a coverslip. The samples were analyzed using CLSM. To analyze ex vivo tumor penetration,[22a] we sacrificed HeLa tumor-bearing mice and collected the tumors when the average tumor volume had reached 300–400 mm. Whole tumors were cultured ex vivo for 24 h with PNV (1 mg mL^{-1}) in medium adjusted to pH 6.5 or pH 7.4. Tumor sections (20 μm thick) were harvested by cryostat, and the edge and inside area of each tumor section were imaged using confocal laser scanning microscopy (Zeiss Ism 510 due, BD). To analyze in vivo tumor penetration, we injected tumor-bearing mice with Dox-loaded conjugates and PNV at a dose of 5 mg Dox kg^{-1} of mouse body weight. At 48 h later, mice were sacrificed and the central part of tumor sections was sectioned at a thickness of 10 μm. Sections were fixed with 4% paraformaldehyde, nuclei were stained with DAPI, and sections were imaged by confocal microscopy. For evaluation of penetration of nanovehicle in tumor spheroids, HeLa multicellular tumor spheroids were prepared as described,[16] then treated with PNV (1 mg mL^{-1}) in PBS buffer at pH 6.5 or 7.4 for 4 h at 37 °C. After the spheroids were rinsed twice with cold PBS followed by fixation with 4% paraformaldehyde for 15 min, they were analyzed by confocal microscopy.

Cellular Uptake and Subcellular Distribution: For quantitative study of nanovehicle uptake by flow cytometry, HeLa cells were seeded onto 12-well plates at a density of 1 × 10^5 cells per well. After incubation for 24 h, cells were treated with Dox-loaded PNV(equivalent Dox dose, 10 μg mL^{-1}) at 37 °C for 2 h. Then medium was removed and cells were harvested. The samples were washed with PBS three times, then immediately analyzed by flow cytometry. The mean fluorescence intensity of 1×10^4 cells was recorded for each sample. For confocal microscopy imaging, HeLa cells were seeded onto coverslips in 24-well plates at a density of 2×10^4 cells/well and incubated for 24 h at 37 °C. Cells were incubated with the Dox-loaded PNV or conjugates at an equivalent Dox concentration of 10 μg mL^{-1} in fresh culture medium at pH 7.4 or pH 6.5 for 2 or 4 h with or without 2 h pretreatment with 50×10^{-3} M NH_4Cl. After incubation at 37 °C, cells were washed twice with ice-cold PBS and then counterstained with Lysotracker Green/Blue to label acidic organelles or with DAPI to label cell nuclei according to the manufacturer's instructions. Then coverslips were mounted on slides and analyzed by confocal fluorescence microscopy.

Nuclear Dox Quantization: Quantization was performed as described.[30] HeLa cells were treated with the various conjugates (equivalent Dox dose,10 μg mL^{-1}) for 4 h, then typsinized, and suspended at a concentration of 5×10^6 cells mL^{-1} for 10 min at 4 °C in a 100×10^{-3} M NaCl solution with 1×10^{-3} M EDTA, 1% Triton X-100, and 10×10^{-3} M Tris buffer (pH 7.4). The suspension was then centrifuged (15 min, 800× g), and the pellet (nuclei) was separated from the supernatant (cytosol). Dox was extracted from each fraction by treatment in methanol at 4 °C overnight. Following centrifugation, the supernatant was collected and used for fluorescent Dox determination.

Cytotoxicity Assay: The cytotoxicity of Dox-loaded conjugates against HeLa cells was evaluated using the MTT assay. HeLa cells were seeded onto 96-well plates at a density of 7×10^3 cells per well and incubated for 24 h. After treatment with Dox-loaded conjugates for 24 h at 37 °C, medium was removed and cells were washed twice with ice-cold PBS. Afterward, cells were incubated for 3 h with MTT (5 mg mL^{-1}, 20 μL per well). Then the supernatant was removed before adding dimethyl sulfoxide (150 μL per well) into the wells to dissolve the formazane of MTT. Absorption at 570 nm was measured using an ELISA plate reader (Bio-Rad, Microplate Reader 550), and cell viability was calculated.

In Vivo Anticancer Efficacy: HeLa tumor-bearing nude mice were randomly divided into five groups ($n = 5$ per group) and intravenously injected with PNV or conjugates on day 0 and day 8 at a dose of 5 mg Dox kg^{-1} of mouse body weight. Tumor width and length were measured every 3 d from day 1, and tumor size was calculated following the formula: (length × $width^2$)/2. Curves showing tumor growth over three weeks were generated.

Supporting Information

Supporting Information is available from the Wiley Online Library or from the author.

Acknowledgements

This study was supported by the National Natural Science Foundation of China (81473167) and the Doctoral Fund of the Ministry of Education of China (2013018111001).

Received: March 28, 2015
Revised: May 5, 2015

---

[1] a) S. Barua, S. Mitragotri, *Nano Today* **2014**, *9*, 223; b) K. A. Whitehead, R. Langer, D. G. Anderson, *Nat. Rev. Drug Discovery* **2009**, *8*, 129; c) M. Sui, W. Liu, Y. Shen, *J. Controlled Release* **2011**, *155*, 227.
[2] a) Q. Sun, M. Radosz, Y. Shen, *J. Controlled Release* **2012**, *164*, 156; b) L. Qiu, T. Chen, I. Ocsoy, E. Yasun, C. Wu, M. You, D. Han, J. Jiang, R. Yu, W. Tan, *Nano Lett.* **2015**, *15*, 457; c) Y. Fan, C. Li, H. Cao, F. Li, D. Chen, *Biomaterials* **2012**, *33*, 4220.
[3] S. D. Perrault, C. Walkey, T. Jennings, H. C. Fischer, W. C. Chan, *Nano Lett.* **2009**, *9*, 1909.
[4] R. K. Jain, T. Stylianopoulos, *Nat. Rev. Clin. Oncol.* **2010**, *7*, 653.
[5] C. Wong, T. Stylianopoulos, J. Cui, J. Martin, V. P. Chauhan, W. Jiang, Z. Popovic, R. K. Jain, M. G. Bawendi, D. Fukumura, *Proc. Natl. Acad. Sci. U.S.* **2011**, *108*, 2426.
[6] a) S. Kunjachan, R. Pola, F. Gremse, B. Theek, J. Ehling, D. Moeckel, B. Hermanns-Sachweh, M. Pechar, K. Ulbrich, W. E. Hennink, G. Storm, W. Lederle, F. Kiessling, T. Lammers, *Nano Lett.* **2014**, *14*, 972; b) H. Cabral, Y. Matsumoto, K. Mizuno, Q. Chen, M. Murakami, M. Kimura, Y. Terada, M. R. Kano, K. Miyazono, M. Uesaka, N. Nishiyama, K. Kataoka, *Nat. Nanotechnol.* **2011**, *6*, 815.
[7] a) Q. He, J. Shi, *Adv. Mater.* **2014**, *26*, 391; b) E. Jin, B. Zhang, X. Sun, Z. Zhou, X. Ma, Q. Sun, J. Tang, Y. Shen, E. Van Kirk, W. J. Murdoch, M. Radosz, *J. Am. Chem. Soc.* **2013**, *135*, 933.
[8] a) E. Oh, J. B. Delehanty, K. E. Sapsford, K. Susumu, R. Goswami, J. B. Blanco-Canosa, P. E. Dawson, J. Granek, M. Shoff, Q. Zhang, P. L. Goering, A. Huston, I. L. Medintz, *ACS Nano* **2011**, *5*, 6434; b) S. Huo, S. Jin, X. Ma, X. Xue, K. Yang, A. Kumar, P. C. Wang, J. Zhang, Z. Hu, X. J. Liang, *ACS Nano* **2014**, *8*, 5852; c) K. Huang, H. Ma, J. Liu, S. Huo, A. Kumar, T. Wei, X. Zhang, S. Jin, Y. Gan, P. C. Wang, S. He, X. Zhang, X. J. Liang, *ACS Nano* **2012**, *6*, 4483.
[9] J. Callahan, P. Kopeckov, J. Kopecek, *Biomacromolecules* **2009**, *10*, 1704.
[10] C. Zhou, M. Long, Y. Qin, X. Sun, J. Zheng, *Angew. Chem., Int. Ed.* **2011**, *50*, 3168.
[11] L. Pan, Q. He, J. Liu, Y. Chen, M. Ma, L. Zhang, J. Shi, *J. Am. Chem. Soc.* **2012**, *134*, 5722.
[12] a) S. R. Schwarze, A. Ho, A. Vocero-Akbani, S. F. Dowdy, *Science* **1999**, *285*, 1569; b) D. Sarko, B. Beijer, R. Garcia, E. M. Nothelfer, K. Leotta, M. Eisenhut, A. Altmann, U. Haberkorn, W. Mier, *Mol. Pharmaceutics* **2010**, *7*, 2224.
[13] L. Pan, J. Liu, Q. He, J. Shi, *Adv. Mater.* **2014**, *26*, 6742.
[14] a) J. Z. Du, X. J. Du, C. Q. Mao, J. Wang, *J. Am. Chem. Soc.* **2011**, *133*, 17560; b) M. Zan, J. Li, S. Luo, Z. Ge, *Chem. Commun.* **2014**, *50*, 7824.
[15] Z. Zhou, L. Li, Y. Yang, X. Xu, Y. Huang, *Biomaterials* **2014**, *35*, 6622.
[16] L. Li, Q. Yang, Z. Zhou, J. Zhong, Y. Huang, *Biomaterials* **2014**, *35*, 5171.
[17] a) J. W. Wojtkowiak, D. Verduzco, K. J. Schramm, R. J. Gillies, *Mol. Pharmaceutics* **2011**, *8*, 2032; b) J. Xiao, X. Duan, Q. Yin, Z. Zhang, H. Yu, Y. Li, *Biomaterials* **2013**, *34*, 9648.
[18] S. Aroui, S. Brahim, M. D. Waard, A. Kenani, *Biochem. Biophys. Res. Commun.* **2010**, *391*, 419.
[19] Y. Y. Yuan, C. Q. Mao, X. J. Du, J. Z. Du, F. Wang, J. Wang, *Adv. Mater.* **2012**, *24*, 5476.
[20] K. J. Chen, Y. L. Chiu, Y. M. Chen, Y. C. Ho, H. W. Sung, *Biomaterials* **2011**, *32*, 2586.
[21] a) T. Etrych, P. Chytil, T. Mrkvan, M. Sirova, B. Rihova, K. Ulbrich, *J. Controlled Release* **2008**, *132*, 184; b) T. Etrych, L. Kovar, J. Strohalm, P. Chytil, B. Rihova, K. Ulbrich, *J. Controlled Release* **2011**, *154*, 241.
[22] a) L. Tang, N. P. Gabrielson, F. M. Uckun, T. M. Fan, J. Cheng, *Mol. Pharm.* **2013**, *10*, 883; b) Y. Yu, X. Zhang, L. Qiu, *Biomaterials* **2014**, *35*, 3467; c) J. J. Li, Y. Han, Q. X. Chen, H. D. Shi, S. U. Rehman, M. Siddiq, Z. S. Ge, S. Y. Liu, *J. Mater. Chem. B* **2014**, *2*, 1813.
[23] P. L. Paine, L. C. Moore, S. B. Horowitz, *Nature* **1975**, *254*, 109.
[24] J. Y. Zhu, Q. Lei, B. Yang, H. Z. Jia, W. X. Qiu, X. Wang, X. Zeng, R. X. Zhuo, J. Feng, X. Z. Zhang, *Biomaterials* **2015**, *52*, 281.

[25] a) M. Tijerina, P. Kopeckova, J. Kopecek, *Pharm. Res.* **2003**, *20*, 728; b) A. Nori, K. D. Jensen, M. Tijerina, P. Kopeckova, J. Kopecek, *Bioconjugate Chem.* **2003**, *14*, 44.

[26] J. M. Rosenholm, A. Meinander, E. Peuhu, R. Niemi, J. E. Eriksson, C. Sahlgren, M. Linden, *ACS Nano* **2009**, *3*, 197.

[27] a) A. G. Tkachenko, H. Xie, D. Coleman, W. Glomm, J. Ryan, M. F. Anderson, S. Franzen, D. L. Feldheim, *J. Am. Chem. Soc.* **2003**, *125*, 4700; b) M. A. van der Aa, G. A. Koning, C. d'Oliveira, R. S. Oosting, K. J. Wilschut, W. E. Hennink, D. J. Crommelin, *J. Gene Med.* **2005**, *7*, 208.

[28] P. Mohan, N. Rapoport, *Mol. Pharm.* **2010**, *7*, 1959.

[29] Y. Yang, Y. Yang, X. Xie, X. Cai, H. Zhang, W. Gong, Z. Wang, X. Mei, *Biomaterials* **2014**, *35*, 4368.

[30] a) J. N. Liu, W. Bu, L. M. Pan, S. Zhang, F. Chen, L. Zhou, K. L. Zhao, W. Peng, J. Shi, *Biomaterials* **2012**, *33*, 7282; b) L. Pan, J. Liu, Q. He, L. Wang, J. Shi, *Biomaterials* **2013**, *34*, 2719.